Monthly Notices of the ROYAL ASTRONOMICAL SOCIETY

MNRAS **500,** 3579–3593 (2021) doi:10.1093/mnras/staa3106
Advance Access publication 2020 October 9

Resolving the Disc–Halo Degeneracy – II: NGC 6946

S. Aniyan,[1] A. A. Ponomareva,[1,2,3★] K. C. Freeman,[1★] M. Arnaboldi,[4★] O. E. Gerhard,[5] L. Coccato,[4] K. Kuijken[6] and M. Merrifield[7]

[1]Research School of Astronomy & Astrophysics, Australian National University, Canberra, ACT 2611, Australia
[2]Oxford Astrophysics, University of Oxford, Denys Wilkinson Building, Keble Rd, Oxford OX1 3RH, UK
[3]Kapteyn Astronomical Institute, University of Groningen, Postbus 800, NL-9700 AV Groningen, the Netherlands
[4]European Southern Observatory, Karl-Schwarzschild-Strasse 2, D-85748 Garching, Germany
[5]Max-Planck-Institut für Extraterrestrische Physik, Giessenbachstrasse, D-85741 Garching, Germany
[6]Leiden Observatory, Leiden University, Niels Bohrweg 2, NL-2333 CA Leiden, the Netherlands
[7]School of Physics and Astronomy, University of Nottingham, University Park, Nottingham NG7 2RD, UK

Accepted 2020 October 6. Received 2020 October 6; in original form 2019 August 14

ABSTRACT

The mass-to-light ratio (*M*/*L*) is a key parameter in decomposing galactic rotation curves into contributions from the baryonic components and the dark halo of a galaxy. One direct observational method to determine the disc *M*/*L* is by calculating the surface mass density of the disc from the stellar vertical velocity dispersion and the scale height of the disc. Usually, the scale height is obtained from near-IR studies of edge-on galaxies and pertains to the older, kinematically hotter stars in the disc, while the vertical velocity dispersion of stars is measured in the optical band and refers to stars of all ages (up to ∼10 Gyr) and velocity dispersions. This mismatch between the scale height and the velocity dispersion can lead to underestimates of the disc surface density and a misleading conclusion of the submaximality of galaxy discs. In this paper, we present the study of the stellar velocity dispersion of the disc galaxy NGC 6946 using integrated star light and individual planetary nebulae as dynamical tracers. We demonstrate the presence of two kinematically distinct populations of tracers that contribute to the total stellar velocity dispersion. Thus, we are able to use the dispersion and the scale height of the same dynamical population to derive the surface mass density of the disc over a radial extent. We find the disc of NGC 6946 to be closer to maximal with the baryonic component contributing most of the radial gravitational field in the inner parts of the galaxy ($V_{\rm max}(\rm bar) = 0.76(\pm 0.14)V_{\rm max}$).

Key words: galaxies: evolution – galaxies: kinematics and dynamics – galaxies: spiral – dark matter.

1 INTRODUCTION

The ‘disc–halo’ degeneracy is an important issue when decomposing H I rotation curves of galaxies, where the contribution from the baryonic matter is mostly determined by the stellar mass-to-light ratio (*M*/*L*). Unfortunately, the *M*/*L* is uncertain due to the challenges involved in traditional methods used to determine it (van Albada et al. 1985; Maraston 2005; Conroy, Gunn & White 2009). Accurate rotation curve decomposition is crucial in determining the potential of a galaxy and the parameters of its dark matter (DM) halo. The densities and scale radii of dark haloes are known to follow well-defined scaling laws and can therefore be used to measure the redshift of assembly of haloes of different masses (Macciò et al. 2013; Kormendy & Freeman 2016; Somerville et al. 2018).

A rather direct observational technique of measuring the disc *M*/*L* is from its surface mass density, which can be estimated from the vertical velocity dispersion and the vertical scale height of the disc (van der Kruit & Freeman 1984; Bottema, van der Kruit & Freeman 1987; Herrmann et al. 2008; Bershady et al. 2010a). The 1D Jeans equation in the vertical direction can be used to estimate the surface mass density (Σ) of the disc via the relation:

$$\Sigma = f\sigma_z^2/Gh_z, \tag{1}$$

where h_z is the vertical scale height, σ_z is the integrated vertical velocity dispersion of the exponential disc, G is the gravitational constant, and f is a geometric factor, known as the vertical structure constant, that depends weakly on the adopted vertical structure of the disc. Having estimated Σ, we can infer stellar mass surface density ($\Sigma_\star$) and the *M*/*L* as $\Upsilon_\star = \Sigma_\star/\mu$, where μ is the surface brightness of a galaxy in physical units ($L_\odot$ pc^2), thus breaking the disc–halo degeneracy.

In Aniyan et al. (2018, hereafter An18), we argued that for the Jeans equation (equation 1) to work effectively, the scale height and dispersions must refer to the same population of stars, and in this case the σ_z is expected to fall exponentially with twice the galaxy scale length. However, usually the vertical dispersions are obtained from measurements of near-face-on galaxies in the optical bands, whereas the scale heights are obtained from studies of edge-on galaxies in the red and near-IR bands (Kregel, van der Kruit & de Grijs 2002).[1]

★ E-mail: anastasia.ponomareva@physics.ox.ac.uk (AAP); kenneth.freeman@anu.edu.au (KCF); marnabol@eso.org (MA)

[1]See also Kregel, van der Kruit & Freeman (2005) for a detailed study of the correlation between the intrinsic properties of edge-on galaxies, i.e. central surface brightness, scale length, and scale height in the *I* band.

Thus, the spectra of star-forming face-on disc galaxies include light from the younger, kinematically colder population of stars. On the other hand, the scale heights obtained from observations of edge-on discs are primarily for the kinematically hotter stars that are above the dust lane in the galaxies. This mismatch can lead to the surface mass density being underestimated which can in turn lead to galaxies' discs being incorrectly classified as submaximal. This issue has plagued most of the previous measurements of the surface mass density of face-on discs (Herrmann & Ciardullo 2009b; Bershady et al. 2011).

In An18, we used integrated light data as well as planetary nebulae (PNe) as tracers of the kinematics of the disc in the face-on spiral NGC 628 to demonstrate the presence of two kinematically distinct populations of disc stars in this galaxy. We also showed the effect of the cold layer on the total surface mass density of the disc (see appendix in An18). This is based on an exact solution for an isothermal sheet of older stars with an embedded very thin layer of younger stars and gas. Its density distribution is a modified version of the familiar $\mathrm{sech}^2(z/2h_z)$ distribution. Following this solution, equation (1) becomes

$$\Sigma_\mathrm{T} = \Sigma_\mathrm{D} + \Sigma_{\mathrm{C},*} + \Sigma_{\mathrm{C,gas}} = \sigma_z^2/(2\pi G h_z), \tag{2}$$

where Σ_T is the total surface density of the disc and Σ_D is the surface density of the older stellar component which is used as the dynamical tracer (its scale height is h_z and its isothermal vertical velocity dispersion is σ_z). $\Sigma_{\mathrm{C},*}$ and $\Sigma_{\mathrm{C,gas}}$ are the surface densities of the cold thin layers of young stars and gas, respectively. An independent measurement of $\Sigma_{\mathrm{C,gas}}$ is available from 21-cm and mm radio observations. As a result, in An18 we showed that the disc which was primarily considered submaximal (Herrmann & Ciardullo 2009b) appears maximal with $V_\mathrm{baryonic} = (0.78 \pm 0.11)V_\mathrm{max}$.

In this paper, we extend our previous work to describe the kinematics of the nearby disc galaxy NGC 6946 with the purpose to establish the method's general viability. The choice of NGC 6946 is motived by its inclination (∼37°), as it is not as face-on as NGC 628, which allows us to derive a more reliable rotation curve, as well as makes more targets accessible for the analysis. We observe NGC 6946 with the VIRUS-W integral field unit spectrograph in the inner regions (30–125 arcsec) to study stellar kinematics through the absorption lines, and with the Planetary Nebula Spectrograph (PN.S), which allows us to study the kinematics of the stellar component in galaxies at low surface brightness values in ellipticals (Pulsoni et al. 2018), lenticulars (Cortesi et al. 2013), and discs (An18) using PNe as discrete tracers out to large radii. The use of PNe to map kinematics to large radii in discs showed the presence of a cold younger disc and a older hotter thicker disc in the Andromeda galaxy in the radial range 14–28 kpc (Bhattacharya et al. 2019). NGC 6946 is a nearby (D = 6.1 Mpc, 1 arcsec = 29.6 pc) disc galaxy with a high star formation rate (SFR = 4.8 $\mathrm{M}_\odot\,\mathrm{yr}^{-1}$ Lee 2006), which is ∼4 times the SFR of NGC 628. This contributes to the importance of the NGC 6946 analysis to access differences between the systems. Unfortunately, the inclination of this galaxy brings in some challenge, as it gets harder to separate the in-plane dispersion components (σ_R and σ_ϕ) from the vertical dispersion (σ_z). However, NGC 6946 is closer than NGC 628, and thus we can achieve higher S/N data for the PNe which helps in our analysis. With the PN.S., PNe in NGC 6946 can be detected and their velocities measured out to 388 arcsec = 11.5 kpc (equivalent to 4.1 disc scale lengths) reaching a surface brightness value of 25 mag in B band.

This paper is organized as follows: Section 2 describes the observations and data reduction for VIRUS-W. Section 3 summarizes the same for the PN.S. Section 4 discusses the photometric properties and derives scale height of the galaxies. Section 5 discusses our analysis to derive the surface mass density of the cold gas in this galaxy. Section 6 presents the analysis involved in the extraction of a double Gaussian model from our data. Section 7 discusses the vertical dispersion profile of the hot and cold stellar components. Section 8 describes the calculation of the stellar surface mass density. Section 9 explains the rotation curve decomposition using the calculated surface mass densities. Section 10 presents our conclusions and scope for future work.

2 VIRUS-W SPECTROGRAPH

2.1 Observations

VIRUS-W is an **Integral Field Unit** (IFU) spectrograph on the 2.7-m telescope at McDonald Observatory designed for relatively high-resolution spectroscopy of low surface brightness regions of galaxies (Fabricius et al. 2012). VIRUS-W observations for NGC 6946 were carried out in 2014 October. We were able to get good quality data for four fields that were positioned on the galaxy at a luminosity weighted radius of about 1 radial scale length along the major and minor axis, and cover the radial extend of up to 175 arcsec which corresponds to ≈20.6 mag arcsec^{-2} in I band, and the surface brightness in the V band (in which the VIRUS-W observations were made) is about a magnitude fainter than the dark V-band sky (see Fig. 4). The positions of the IFU fields are shown in Fig. 1. The coordinates and exposure time at each position are given in Table 1. The observations were carried out in a sky–galaxy–sky observing sequence. This sequence was repeated at least three times at each field, as indicated in Table 1. This enabled very good sky subtraction using the automated pipeline developed for VIRUS-W (see An18 for further details).

We then used the CURE data reduction pipeline (Goessl et al. 2006) to get the sky subtracted 1D spectra at each of the four fields. Since the IFU fields cover a large radial extent of NGC 6946 (Fig. 1), we split the data into two radial bins at luminosity weighted mean radii of 54 and 98 arcsec, respectively. After further processing (see Section 6.1), we obtain a 1D summed spectrum for each radial bin that we use to extract the velocity dispersions from the absorption lines.

3 PLANETARY NEBULA SPECTROGRAPH

3.1 Observations and velocity extraction

The PN.S is a double counter-dispersed wide-field spectrograph designed to discover extragalactic PNe and measure their radial velocities in a single observation, used on the William Herschel Telescope on La Palma (Douglas et al. 2002). The data for NGC 6946 were acquired in 2014 September. The weather during the run was excellent, with typical seeing of ∼1 arcsec. We obtained 11 images centred on the centre of the galaxy, each with an exposure time of 1800 s following the strategy adopted in An18. We use the PN.S data reduction pipeline (Douglas et al. 2007) to get the final stacked 'left' and 'right' image for the [O III] data. The unresolved objects are candidate PNe, and their relative positions on the left and right stacked images give us their radial velocities. We also imaged NGC 6946 in H α, using the H α narrow-band filter on the undispersed H α arm of the PN.S. We then used the [O III] stacked images along with the H α stacked image to identify the PNe candidates in this galaxy.

3.2 Identification of sources

To identify our PNe and separate them from the H II regions which also emit in [O III], we use the luminosity function for all

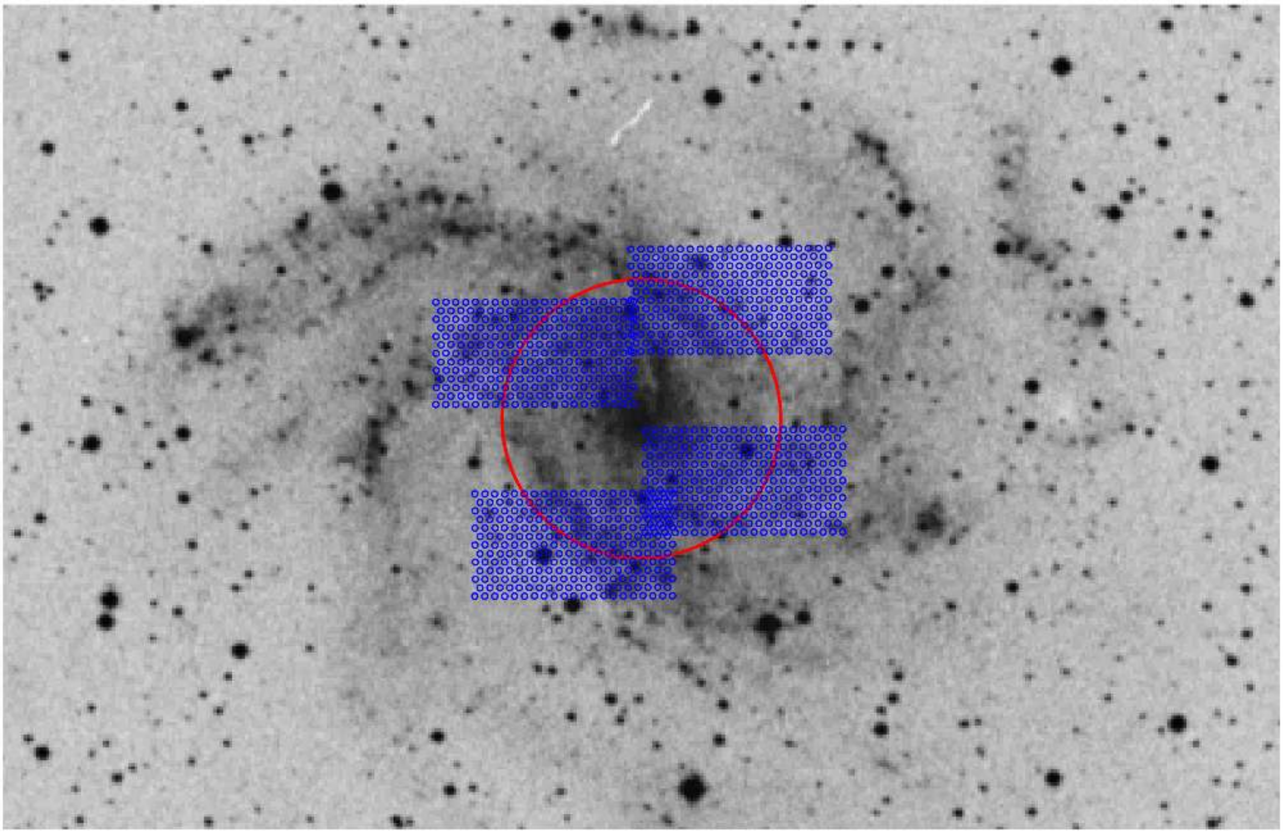

Figure 1. The positions of the four VIRUS-W IFU fields showing the 267 fibres in each field overlaid on a DSS image of NGC 6946. The red circle at a radius of 75 arcsec shows the separation between our inner and outer radial bins.

Table 1. Coordinates and exposure times for the IFU fields.

Galaxy	RA (J2000)	Dec (J2000)	Exposure time (s)
NGC 6946	20:34:54.04	+60:08:04.8	3 × 800
	20:34:47.25	+60:10:23.8	3 × 800
	20:34:47.13	+60:08:48.4	3 × 800
	20:34:56.34	+60:10:01.6	3 × 800

spatially unresolved [O III] emitters identified in the combined left and right images of the PN.S. Then we introduce the expected bright luminosity cut-off for PNe. We include only objects fainter than this value in our analysis. Objects brighter than the cut-off are mostly obvious bright H II regions. For more details please see An18. Consequently, we identified 444 unresolved objects with [O III] emission in this galaxy. From the measured positions of these sources on the left and right images, astrometric positions and line-of-sight (LOS) velocities were derived simultaneously. The typical measurement error associated with the PNe radial velocities is <9 km s^{-1} (see section 3.3 in An18). We then converted our instrumental magnitudes on to the m_{5007} magnitude scale $m_{5007} = m_0 + 25.16$, using our spectrophotometric standards. These magnitudes were corrected for foreground extinction using the Schlafly & Finkbeiner (2011) dust maps. At the distance of NGC 6946, the bright luminosity cut-off for PNe in this galaxy is expected to be at $m_{5007} = 23.22$. Fig. 2 shows the luminosity function for NGC 6946, including all identified unresolved sources. The dashed line in the plot shows the position of the bright luminosity cut-off for the PNe.

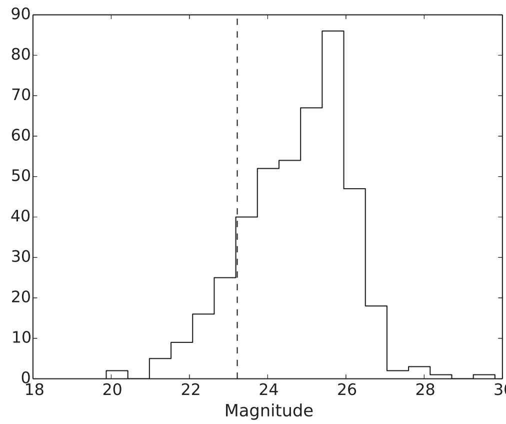

Figure 2. The luminosity function for all spatially unresolved [O III] emitters identified in the combined left and right images of the PN.S for NGC 6946. The dashed line shows the expected bright luminosity cut-off for PNe. Objects brighter than the cut-off are probably bright H II regions.

After the identification of 444 sources, the resulting sample represents a mix of H II regions and PNe since both can have strong [O III] emission. We again use our empirical relationship between the ([O III]–H α) colour and the m_{5007} magnitude to discriminate between PNe and H II regions (Arnaboldi et al., in preparation). Fig. 3 shows the colour–magnitude diagram used to identify PNe. Thus, we obtain 375 unresolved [O III] sources classified as PNe: 125 per each radial bin. Earlier observations by Herrmann & Ciardullo (2009a) found ≈70 PNe candidates in this galaxy.

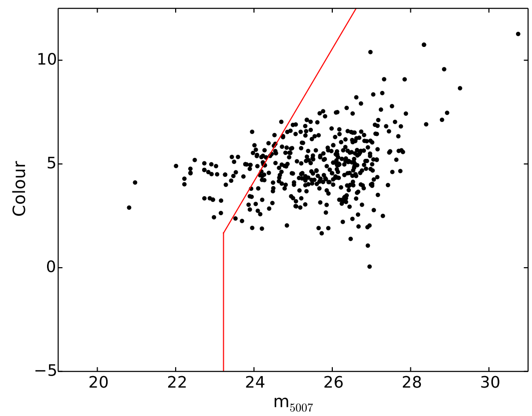

Figure 3. The colour–magnitude plot for [O III] sources in NGC 6946. The vertical axis is the ([O III]–H α) colour and the horizontal axis is the m_{5007} magnitude. The PNe lie to the right of the red lines. Only these objects are used in our analysis.

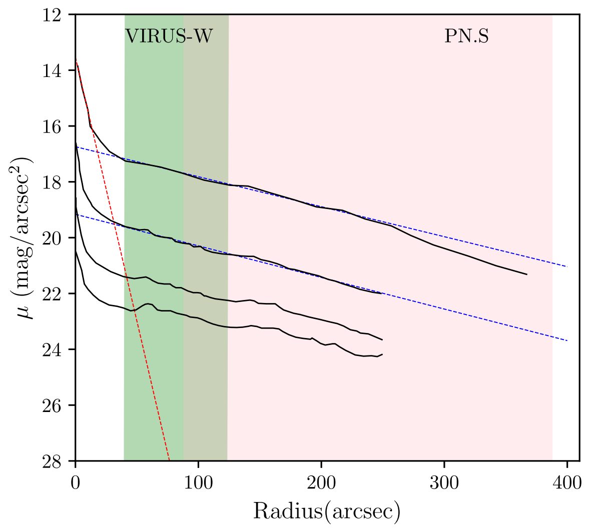

Figure 4. The surface brightness profiles of NGC 6946 in *BVI* (Makarova 1999) and 3.6 μm band (Muñoz-Mateos et al. 2009) are shown from bottom to top. The surface brightness is shown in VEGA magnitudes. The contribution to the light from the stellar disc in *I* band is shown with blue line. The contributions to the total light from bulge and disc in the 3.6 μm band are shown with red and blue lines, respectively. The average error on the surface brightness is ∼0.01 mag for the 3.6 μm band and ∼0.02 mag in the optical bands. The radial extent of the Virus-W and PNS data is shown with green and pink bands, respectively.

In addition to H II regions, the historical supernovae are a potential source of contamination which can bias the PNe luminosity function (Kreckel et al. 2017). According to the IAU Central Bureau for Astronomical Telegrams (CBAT) List of Supernovae, there are nine known historical supernovae in NGC 6946, which is an unusually high number. However, none of these objects made it into our PNe sample. We had one unresolved [O III] source at ∼3 arcsec from the historical supernova SN 2002hh. Yet, this object was classified as an H II region after applying our colour–magnitude cut. Thus, we do not have any of these contaminants in our final PNe sample.

4 PHOTOMETRY AND SCALE HEIGHT

NGC 6946 is a late-type spiral galaxy that shows the presence of a small bulge. Fig. 4 shows the surface brightness profiles of NGC 6946 in four photometrical bands: *BVI* from Makarova (1999) and 3.6 μm from Muñoz-Mateos et al. (2009). We use spatial information from these profiles later in the paper to calculate the *M*/*L* ratio as a function of radius. We also use the 3.6 μm profile to perform bulge–disc decomposition (shown with red and blue lines in Fig. 4) in order to account for the bulge contribution during the mass modelling.

The disc scale height (h_z) cannot be directly measured for face-on galaxies. Thus, the scaling relation between the scale height and scale length (h_R) of spiral galaxies is often used to infer h_z of a face-on system. Kregel et al. (2002) studied the scale heights of a sample of edge-on galaxies in the *I* band and found strong correlations with the scale lengths. The use of the *I* band is justified as it is not sensitive to the contribution of dust and PAHs, and it traces the older thicker stellar disc population. Bershady et al. (2010b) found that $\log(h_R/h_z) = 0.367\log(h_R/\mathrm{kpc}) + 0.708 \pm 0.095$ by fitting the data from Kregel et al. (2002).[2] Thus, using the disc fit to the *I*-band surface brightness profile (Fig. 4) we measure the disc scale length to be equal to 95 arcsec or 2.8 kpc. Throughout the paper, we adopt the distance to the galaxy $D = 6.1 \pm 0.6$ Mpc from Herrmann et al. (2008) to be consistent with our previous study of NGC 628 (An18). We note that this distance is a bit smaller than the distance determined by Anand, Rizzi & Tully (2018) (7.72 ± 0.32 Mpc) who used the tip of the giant branch method. Finally, we obtain the scale height of the disc $h_z = 376 \pm 75$ pc. We use this value throughout the paper when we refer to the calculation of the surface mass density and mass modelling. Following de Grijs, Peletier & van der Kruit (1997), we assume that the scale height h_z for the disc of this late-type spiral is independent of the galactic radius.

[2]Bershady et al. (2010b) scaling is used to convert the scale length into scale height for an old population of stars.

Table 2. Photometrical and geometrical parameters of NGC 6946 measured from the literature data and adopted in the analysis throughout the paper with the associated error. The average error on the surface brightness is ∼0.01 mag for the 3.6 μm band and ∼0.02 mag for the *I* band.

Parameters	Value
Scale length (*I* band)[a]	95.0 ± 5 arcsec
Scale length (3.6 μm band)[b]	92.0 ± 1 arcsec
μ_0 [I]	19.16 mag arcsec^{-2}
μ_0 [3.6]	16.74 mag arcsec^{-2}
Scale height (*I* band)	376 ± 75 pc
Distance[c]	6.1 ± 0.6 Mpc
H I inclination[d]	37° ± 7°
H I position angle[d]	242° ± 10°

Note. Data from the literature:
[a]Makarova (1999);
[b]Muñoz-Mateos et al. (2009);
[c]Herrmann et al. (2008);
[d]Walter et al. (2008).

Table 2 summarizes the values of the various parameters of this galaxy that we use in our analysis of the surface mass density and mass modelling. Inclination and position angles (PA) are measured with the tilted-ring modelling of the THINGS H I data (Walter et al. 2008; see Section 9.1). These values agree well with the values obtained from the PNe. This indicates that there is no evident disconnect between the gaseous H I disc and the stellar disc, at least within our covered radii.

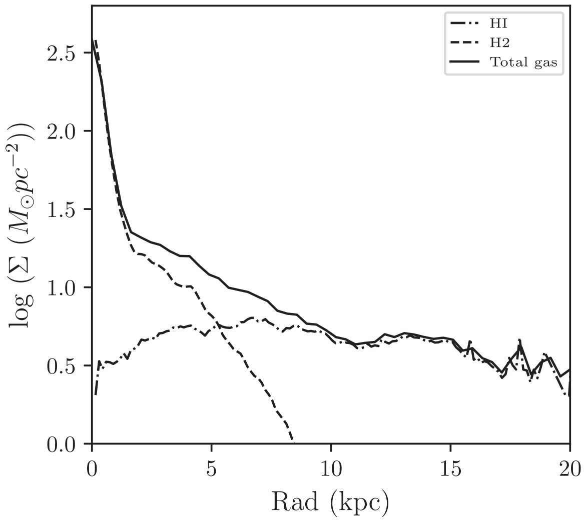

Figure 5. Surface mass density of the cold gas (atomic and molecular) in NGC 6946. The H I density profile derived from THINGS data (Walter et al. 2008) is shown with the dot–dashed line. H2 profile derived from the HERACLES data (Leroy et al. 2009) is shown as the long-dashed curve. The surface density profile of the total gas is shown as the solid curve. All profiles are corrected for contribution from helium and heavier elements by a factor of 1.4.

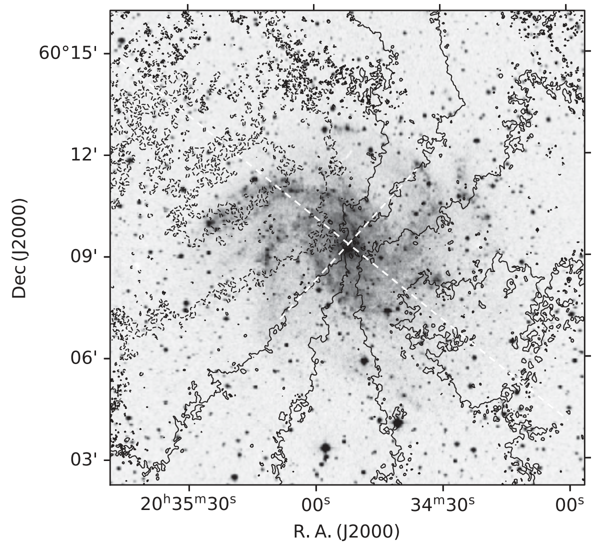

Figure 6. The DSS image of NGC 6946 with the overlapped velocity contours from the H I velocity field. The orientation of the major and minor axis of the H I disc is shown with the dashed lines. Velocity separation of the contours is 40 km s^{-1}.

5 SURFACE MASS DENSITIES OF COLD GAS

To account for the gas contribution to the measured total surface mass density, and to able to separate stellar from gaseous components, we derive total cold gas surface density using H I data from the THINGS survey (Walter et al. 2008) and CO data from the HERACLES survey (Leroy et al. 2009).

The H I radial surface density profile was derived from the integrated column-density H I map, constructed by summing the primary beam corrected channels of the clean data cube. We use the same radial sampling, position, and inclination as for the tilted ring modelling (Section 9.1). The resulting flux (Jy beam^{-1}) was converted to mass densities (M$_\odot$ pc^{-2}) using equations (5) and (6) in Ponomareva, Verheijen & Bosma (2016). The error on the H I surface mass density was determined as the difference in the profile between approaching and receding sides of the galaxy, and does not exceed $\sim$0.4 M$_\odot$ pc^{-2}.

The H_2 surface mass density profile was obtained from the CO total intensity map with the same radial sampling, position, and inclination angles as for the H I profile. The resulting CO intensities were converted into the H_2 surface mass density using the prescription by Leroy et al. (2009). The error on the H_2 surface mass density was obtained from the HERACLES error maps and does not exceed $\sim$0.7 M$_\odot$ pc^{-2}.

The resulting H I and H_2 surface mass density profiles together with the total cold gas profile are shown in Fig. 5 with dot–dashed, long-dashed, and solid curves, respectively. All profiles are corrected for the presence of metals and helium and deprojected so as to be face-on. It is worth mentioning the large amount of molecular gas in NGC 6946, which significantly dominates the amount of atomic gas in the inner parts. We note that Crosthwaite & Turner (2007) find similar results and report the total H_2 mass to be equal to 3×10^9 M$_\odot$, approximately one-third of the total interstellar hydrogen gas mass.

6 EXTRACTING VELOCITY DISPERSIONS OF THE HOT AND COLD COMPONENTS

In this section, we describe in detail the procedure of extracting accurate velocity dispersions of two stellar components. We present the different techniques used to derive dispersions from the stellar absorption line spectra in the inner parts, and from the PNe data in the outer regions.

6.1 Stellar absorption spectra

6.1.1 Removing galactic rotation

To remove the galactic rotation and to get rid of any large-scale streaming motions across the IFU, we measure the local H I velocity at the position of each fibre from the THINGS data (Walter et al. 2008) and shift each fibre spectrum by this local H I velocity. Fig. 6 shows the DSS image of NGC 6946 with the overlapped velocity contours from the H I velocity field. We note that our IFU observations lie within the stellar disc of the galaxy, as shown in Fig. 1, while the H I disc is more extended. This method proved to be preferable to removing the galactic rotation by modelling the rotation field over the entire IFU using the observed rotation curve, as the latter gives larger LOS velocity dispersions ($\sigma_{\rm LOS}$). However, our technique introduces an additional small velocity dispersion component from the H I itself, for which a correction is needed (see Section 6.1.2).

The VIRUS-W IFU covers a large radial extent of the galaxy. Since the vertical velocity dispersion (σ_z) is expected to fall exponentially with twice the galaxy's scale length, we do not want each radial bin to be too large. We divide our IFU data into two radial bins corresponding to luminosity weighted mean radii of 54 and 98 arcsec. The stellar component tends to rotate more slowly than the gaseous component and neglecting this effect can lead to overestimated $\sigma_{\rm LOS}$. NGC 6946 has an inclination of 37°, so this asymmetric drift may affect the measurement significantly. To remove the effects of differential asymmetric drift, we split the 267 fibres in each IFU field into a grid of six cells, each with about 44 fibres. The gradient in asymmetric drift is negligible across the small area of a cell. We sum the spectra from all fibres in a cell and cross-correlate five of the summed spectra against the sixth. This gives the shift in velocity to apply to the five spectra to match the spectrum from the sixth grid. This procedure gets rid of any differential asymmetric drift across the

IFU fields. We repeat this exercise for all four IFU fields. The cross-correlated, asymmetric-drift-corrected spectra were then shifted to redshift $z = 0$, before summing up to the final spectra. This approach has its caveats, as the hot and cold disc components will have slightly different asymmetric drifts. The difference in asymmetric drift between the hot and cold components is 5 $\mathrm{km\,s^{-1}}$ evaluated at the mean radius for the inner VIRUS-W region and 6 $\mathrm{km\,s^{-1}}$ for the outer region. At 37° inclination, these differences become 3 and 4 $\mathrm{km\,s^{-1}}$, respectively. These values are uncertain because of the observation errors in the dispersion, but seem unlikely to make a significant contribution to the measured velocity dispersions. Although this effect is expected to be minor for a galaxy with an inclination of 37°, it could be an issue for more inclined galaxies.

The final summed spectra from the inner and outer radial bins, respectively, have an SNR of 105 and 77 per wavelength pixel (each wavelength pixel is ∼0.19 Å; the resolving power R = 8700, so the Gaussian σ of the PSF is 14.7 $\mathrm{km\,s^{-1}}$). We only use the region between wavelengths of about 5050–5300 Å in our analysis, since it has the highest resolution and avoids the emission lines at lower wavelengths. The [N I] doublet emission lines together with the third peak can be seen at ∼5200 Å (see Fig. 7). Although we exclude the emission-line region from our velocity dispersion fits, the presence of these three lines is unexpected. It is hard to definitely conclude that they come from the galaxy interstellar medium (ISM), because the heliocentric radial velocity of NGC 6946 is only 40 $\mathrm{km\,s^{-1}}$. In An18, NGC 628 (radial velocity 657 $\mathrm{km\,s^{-1}}$) showed the two [N I] emission lines at λ = 5197.9 and λ = 5200.3 Å, and they were clearly at the velocity of the galaxy. The strengths of the two lines are approximately equal. The sky [N I] lines, which typically have line ratios 5198/5200 ∼ 1.7, have been successfully subtracted in the reduction pipeline and do not appear. In NGC 6946, our strategy for removing galactic rotation means that all lines from the galactic plane have velocities near zero, relative to the systemic velocity of the galaxy. We see three emission lines at observed λ 5196.2, 5198.4, 5200.4 Å. Their relative line strengths can be seen in Fig. 7. NGC 6946 is known to have a significant amount of halo H I at velocities up to ±100 $\mathrm{km\,s^{-1}}$, in addition to its planar H I (Boomsma et al. 2008).[3] Thus, we speculate that the three observed lines come from a superposition of two pairs of [N I] lines: a weaker pair at near-systemic velocity from the planar gas, and a stronger pair blueshifted by about 2 Å associated with the negative velocity gas. The superposition of the two pairs gives three lines as observed, with their apparent line ratios.

6.1.2 *LOSVD and the vertical velocity dispersion*

We use PPXF (Cappellari 2017) to obtain the first two moments (the mean LOS velocity and the σ_{LOS}) for the two Gaussians for the two VIRUS-W spectra. We fit two and single Gaussian components to the data for the comparison. The resulting fits are shown in Fig. 7. Further, we use the Bayesian Information Criterion (BIC; Schwarz 1978) to judge the preferred model (one-component or two-component) for the spectra (see equations 3 and 4 in An18 on how to calculate BIC). The BIC applies a penalty for models with a larger number of fitted parameters. Thus, between two models, the model with the lower BIC value is preferred. However, we note that in case of the similar BIC values, the BIC can only be considered as a suggested preference. For our data, the two-component fit is preferred over the single-component fit in both of the radial bins, this result is also consistent with the reduced χ^2. The results for both fits are tabulated in Table 3.

PPXF uses a best-fitting linear combination of stellar templates to directly fit the spectrum in pixel space and to recover the LOS velocity distribution (LOSVD). We observed template stars of different spectral types with VIRUS-W as our list of stellar templates, to avoid resolution mismatch between the stellar templates and the galaxy spectrum. We assume the two components of the LOSVD to be Gaussian for this close-to-face-on galaxy, and therefore retrieved only the first and second moment parameters from PPXF.

PPXF finds an excellent fit to our spectrum, as shown in Fig. 7. It also returns the adopted spectra of the individual components, which are consistent with the spectra of red giants. The mean contributions of the cold and hot disc components to the total light are 52 per cent and 48 per cent in the inner radial bin and 46 per cent and 54 per cent in the outer bin. To correct σ_{LOS} values for the contribution of the H I velocity dispersion, we adopt a correction value to be ∼6 $\mathrm{km\,s^{-1}}$ (see Section 6.1.1).

We then calculate the vertical component of the stellar velocity dispersion σ_z from the LOS component σ_{LOS} using the following equation:

$$\sigma_{\mathrm{LOS}}^2 = \sigma_\theta^2 \cos^2\theta.\sin^2 i + \sigma_R^2 \sin^2\theta.\sin^2 i + \sigma_z^2 \cos^2 i + \sigma_{\mathrm{meas}}^2, \quad (3)$$

where σ_R, σ_θ, and σ_z are the three components of the dispersion in the radial, azimuthal, and vertical direction, σ_{meas} is the measurement error on the velocity, and i is the inclination of the galaxy ($i = 0$ is face-on). Using the epicyclic approximation in the part of the rotation curve that is close to solid body, we adopt $\sigma_R = \sigma_\theta$, and for the part of the rotation curve that is flat, we adopt $\sigma_R = \sqrt{2}\sigma_\theta$. Based on an examination of the THINGS H I velocities along the galaxy's kinematic major axis (last panel in Fig. 12), we determine this galaxy's rotation curve at radius ≤200 arcsec to be solid body and beyond 200 arcsec to have a flat rotation curve. We also adopt the stellar velocity ellipsoid parameter σ_z/σ_R ratio to be 0.6 ± 0.15 following the result from Shapiro, Gerssen & van der Marel (2003). This value is consistent with the value used by Bershady et al. (2010b) and the value found in the solar neighbourhood by Aniyan et al. (2016). For the discussion regarding the uncertainties of σ_z/σ_R measurements for external galaxies and its dependence on the morphological type please see An18, section 5. The uncertainty in σ_z/σ_R is included in the error of σ_z as described in section 7.1.2 of An18. We correct σ_z values for the small broadening introduced by subtracting the local H I velocity to remove galactic rotation. Our results for the stellar σ_z values for both stellar components are presented in Table 3. The errors are the 1σ errors obtained using Monte Carlo simulations. This was done by running 1000 iterations where, in each iteration random Gaussian noise appropriate to the observed SN of the IFU data was added to the best-fitting spectrum originally returned by PPXF. Then, PPXF was run again on the new spectrum produced in each iteration. The errors are the standard deviations of the distribution of values obtained over 1000 iterations.

6.2 Planetary nebulae

6.2.1 *Removing galactic rotation*

From the PNe velocity field, we also remove the effects of galactic rotation, similarly to the analysis of the IFU integrated light absorption spectra. We use H I velocity at the position of each of our PNe from the THINGS first moment map and then subtract local H I velocities from the PNe velocities. These velocities, corrected

[3] We thank the anonymous referee for pointing out the presence of the 'beard' in this galaxy, which is usually associated with the extraplanar gas.

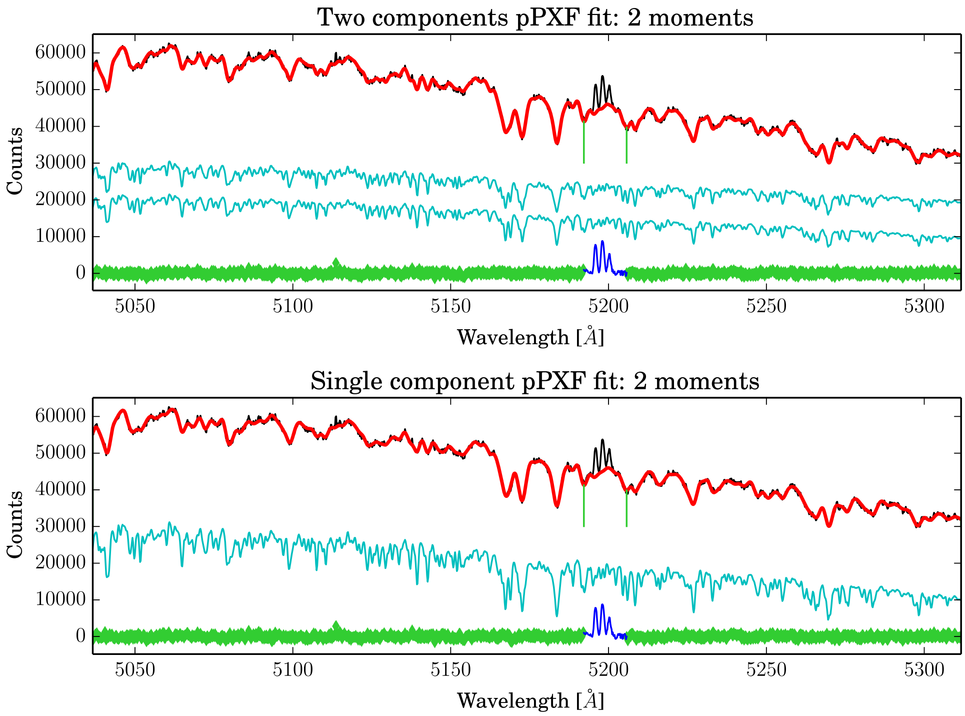

(a)

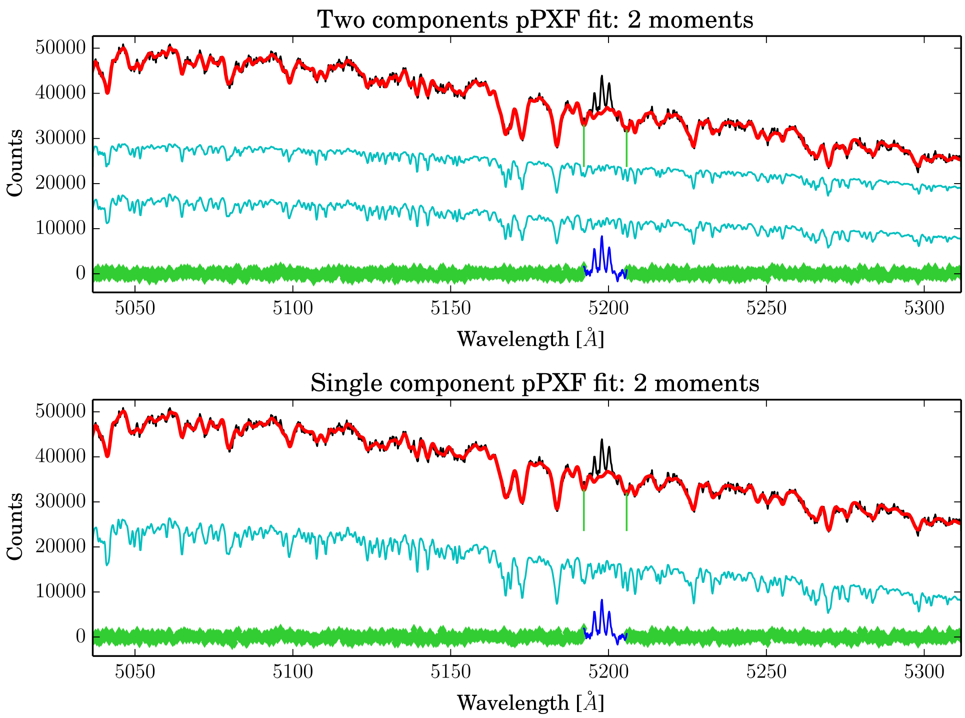

(b)

Figure 7. The PPXF fit results in (a) the inner radial bin at a luminosity weighted mean radius of 54 arcsec and (b) the outer bin at a luminosity weighted mean radius of 98 arcsec. The upper panel shows the two-component fit to the data whereas the lower panel shows a single component fit. Only the high-resolution Mgb region of the spectrum was used for the fit. The galaxy spectrum is in black and the best fit from PPXF is in red. The cyan spectra are the two and one component spectra that PPXF found. The cyan spectra have been shifted vertically so as to be clearly visible. The residuals are shown in green. We note the presence of three peaks in the wavelength range 5196.2–5200.4 Å which we suggest is due to the superposition of the [N I] doublet emissions from outflows in the ISM (Boomsma et al. 2008) to the [N I] doublet emission from the regular rotating ISM, see Section 6.1.1 for additional details. The wavelength region 5196.2–5200.4 Å is omitted from the fit.

Table 3. The single and double Gaussian fit from PPXF. For each component, the table gives the vertical velocity dispersion σ_z for each of the components. Dispersions have been corrected for the contribution from the H I velocity dispersion. An estimate of the reduced χ^2 and the Bayesian Information Criterion parameter BIC is also given. Both the smaller chi-squared and the lower BIC suggest that the two-component model is preferred.

Mean radius	Two-component model				One-component model		
(arcsec)	$\sigma_{z,\text{cold}}$ (km s^{-1})	$\sigma_{z,\text{hot}}$ (km s^{-1})	BIC	χ^2_{red}	σ_z (km s^{-1})	BIC	χ^2_{red}
54	26.6 ± 4.9	65.3 ± 12.1	17164	1.225	39.7 ± 6.3	17283	1.410
98	19.3 ± 3.6	64.6 ± 12.2	17351	1.231	29.3 ± 4.7	17462	1.380

for the galactic rotation, are henceforth denoted v_{LOS}. We use v_{LOS} to calculate the velocity dispersions. As for the VIRUS-W data, the radius and azimuthal angle (θ) of the PNe in the plane of the galaxy were calculated using our estimated PA and angle of inclination, and the v_{LOS} data were then radially binned into three bins, each with about 125 PNe. Fig. 8 shows the v_{LOS} versus θ plots in each radial bin before and after the H I velocities were subtracted off. The distribution of the v_{LOS} after the correction for the H I velocities is shown in Fig. 9 for three radial bins, respectively. The distributions of the data points already suggest the presence of the two kinematically distinct components as it cannot be well fit with the single Gaussian distribution, as shown in Fig. 9, and show a clear indication of a cold kinematic component in v_{LOS} in each radial bin.

6.2.2 LOSVD and the vertical velocity dispersion

In each radial bin, we remove a few obvious outliers, based on a visual inspection of the velocity histogram of the objects. A maximum likelihood estimator (MLE) routine was then used to calculate the LOS velocity dispersions and the subsequent σ_z in each radial bin. The first iteration in this routine estimates σ_{LOS} for the kinematically cold and hot component by maximizing the likelihood for the two-component probability distribution function given by equation (6) in An18.

In order to calculate the surface mass density using equation (2), we need the vertical velocity dispersion of the hot component (σ_z). To determine it, we use a second MLE routine. Two parameters are passed to the function in this stage: σ_{z1} and σ_{z2} which are the vertical velocity dispersions of the cold and hot components, respectively. The σ_{LOS} values obtained using equation (6) in An18 are passed to the routine as initial guesses, since the σ_z will be very close to the value of σ_{LOS} for this galaxy. We assume $f = \sigma_R/\sigma_z = 1.7 \pm 0.42$ (see Section 6.1.2) and use inclination $i = 37°$ (see Section 9.1). The PN.S data for the first radial bin are all at radii <200 arcsec, where the rotation curve is close to solid body. In this bin, we assume the radial and azimuthal components of the velocity dispersion are equal i.e. $\sigma_R = \sigma_\theta$. The PN.S data for the second and third radial bin are all at radii >200 arcsec where the rotation curve is flat and we use: $\sigma_R = \sqrt{2}\sigma_\theta$, where σ_R and σ_θ are the in-plane dispersions in the radial and azimuthal directions. Finally, once the initial guesses are passed to the routine, it calculates the expected σ_{LOS} for the hot and cold component at each azimuthal angle (θ) using the relation:

$$\sigma^2_{\text{LOS1}} = \frac{\sigma^2_{z1} f^2}{2} \cos^2\theta . \sin^2 i + \sigma^2_{z1} f^2 \sin^2\theta . \sin^2 i + \sigma^2_{z1} \cos^2 i .$$

$$\sigma^2_{\text{LOS2}} = \frac{\sigma^2_{z2} f^2}{2} \cos^2\theta . \sin^2 i + \sigma^2_{z2} f^2 \sin^2\theta . \sin^2 i + \sigma^2_{z2} \cos^2 i .$$

The subscripts 1 and 2 refer to the components of the cold and hot populations, respectively. This step depends on the theta-distribution of the PN in each bin. Thus, the routine then proceeds to calculate the probability of a particular v_{LOS} to be present at that azimuthal angle via the equation:

$$P = \frac{N}{\sigma_{\text{LOS1}}\sqrt{2\pi}} \exp\left(\frac{-(\text{v}_{\text{LOS}} - \mu_1 \cos\theta . \sin \text{i})^2}{2\sigma^2_{\text{LOS1}}}\right) + \frac{1-N}{\sigma_{\text{LOS2}}\sqrt{2\pi}} \exp\left(\frac{-(\text{v}_{\text{LOS}} - \mu_2 \cos\theta . \sin \text{i})^2}{2\sigma^2_{\text{LOS2}}}\right) . \quad (4)$$

In equation (4), N is the value of the fraction of the cold population returned by the routine that calculated σ_{LOS} described earlier; μ_1 and μ_2 are associated with the means of the two components; the $\cos\theta.\sin i$ term factors for any asymmetric drift present in the data. Whether we let the code estimate the terms μ_1 and μ_2 or if we fix these terms at 0, it made negligible difference to the dispersions. This shows that there is negligible contribution from the asymmetric drift in the data in each of our radial annuli. Equation (4) is maximized to return the best-fitting values for σ_z for the hot and cold population of PNe. The 1σ errors are calculated similar to the method used in the analysis of the VIRUS-W data. We carry out our Monte Carlo error estimation by using the double Gaussian distribution found by our MLE code, to extract about 125 random velocities (i.e. same number of objects as in each of our bins). We then use this new sample to calculate the σ_z of the hot and cold component using our MLE routines. This whole process was repeated 1000 times, recording the dispersions returned in each iteration. The 1σ error is then the standard deviation of the distribution of the dispersions returned from these 1000 iterations. The vertical velocity dispersions for the two components returned from the MLE routine are given in Table 4. After extracting σ_z from σ_{LOS}, the presence of the cold component seems to remain prominent in bins 1 and 2, but not in bin 3, where the one component model is preferred. However, the distribution of the PNe LOS velocities for bin 3 (Fig. 9) still suggests the presence of the two kinematically distinct components.

The dispersions for the PNe were also corrected for the H I dispersion, similarly to the spectra analysis by quadratically subtracting H I velocity dispersion (~6 km s^{-1}) from the values of the vertical velocity dispersions returned by the MLE routine. This dispersion is evaluated by fitting a plane function to the H I velocities over the IFU and calculating the rms scatter of the H I velocities about this plane. We note that this scatter is not the same as the local H I velocity dispersion as measured from the H I profile width. We also correct the measured dispersions for the measurement errors of the individual PNe, as shown in fig. 3 in An18. The rms measuring error in each radial bin is about 6 km s^{-1}. The formal variance of the corrected cold dispersion value at all PNe radial bins is negative. Hence, we show its 90 per cent confidence upper limit in Fig. 10 and Table 4. We carried out a comprehensive analysis using the

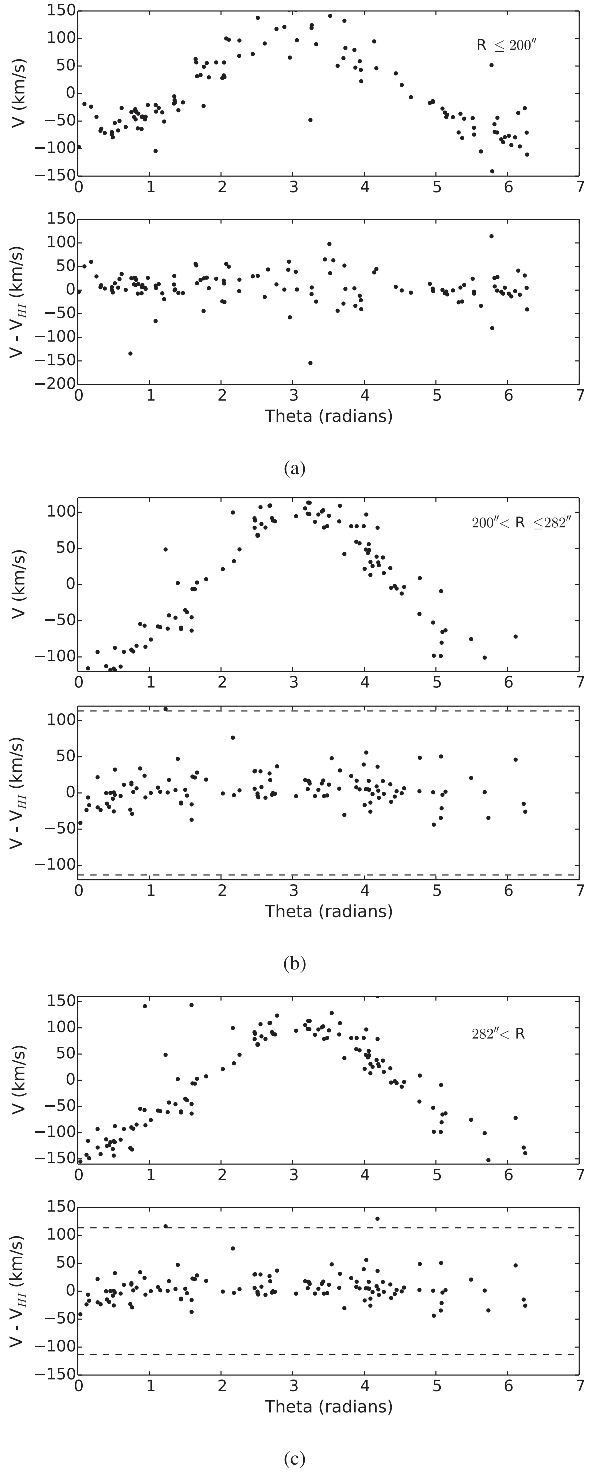

Figure 8. Velocity versus azimuthal angle plots in three radial bins, each with about 125 PNe. The angle θ is in the plane of the galaxy, measured from the line of nodes. The top panels show the velocity before taking off the local THINGS velocity and the bottom panels show the velocities after correcting for galactic rotation. A few outliers were removed based on a visual inspection of the velocity histogram of the objects in each bin. The objects within the dashed lines are the ones that were included in our sample for analysis; no objects were thrown out in the first bin. Each panel shows a mix of cold population of spatially unresolved emission line objects, plus a hotter population whose velocity dispersion appears to decrease with galactic radius.

colour–magnitude cut to discriminate between the H II regions and PNe (Fig. 3). Unfortunately, removing H II contaminants in disc galaxies is very challenging. There is a small probability that we may still have some H II contaminants in our cold component. However, we do not use the dispersion of our cold component in any further analysis. Our aim is to separate out the cold component (whether cold PNe or H II regions) from the kinematically hot component and then use the $\sigma_{z,\,\mathrm{hot}}$ with the scale height for the same population to calculate the surface mass density. Hence, the nature of the objects that contribute to our cold dispersion is irrelevant as long as they are separated out effectively.

7 VERTICAL VELOCITY DISPERSION PROFILE

Fig. 10 shows the velocity dispersion results obtained from the integrated light VIRUS-W data (points at R = 54 and 98 arcsec) and the PNe from the PN.S data (three outer points) in each radial bin. At each radius, we show the one-component dispersion (cyan markers) and then the hot and cold thin disc dispersion from the double Gaussian fit (black and grey markers). The solid curve in Fig. 10 is an exponential fit to the hot component data in the form $\sigma_z(R) = \sigma_z(0)\exp(-R/2h_{\mathrm{dyn}})$, as expected from equation (2) if the total surface density Σ_{T} is exponential in radius and has a radially constant scale height h_z. From this exponential fit, we obtain the best-fitting dynamical scale length to be $h_{\mathrm{dyn}} = 92$ arcsec which is in excellent agreement with the scale length measured for the 3.6 μm band as $I(R) = I(0)\exp(-R/h_{r,[3.6]})$ (Table 2). The fitted central velocity dispersion for the hot component is $\sigma_z(0) = 87.8 \pm 4.9$ km s^{-1}. We recall that it is this hot component dispersion that should be used with the derived scale height from Section 4 to estimate the total surface mass density of the disc. If we assume a single homogeneous population of tracers and fit the same exponential function to the one-component dispersions (cyan markers in Fig. 10), we find the best-fitting dynamical scale length to be $h_{\mathrm{dyn}} = 120$ arcsec and the central vertical dispersion $\sigma_z(0) = 49.2 \pm 5.1$ km s^{-1}, which is ∼50 per cent smaller than the central velocity dispersion from the fit to the hot component. The use of this one-component dispersion for the calculation of the surface mass density would underestimate the surface density by a factor of ∼2, which would be enough to make the maximal disc look submaximal, but with a gradient in the *M*/*L* ratio (see the results from Herrmann & Ciardullo 2009b about the increase in the disc *M*/*L* ratio in the outer disc).

We note that the difference between the one-component dispersions and the hot component dispersions decreases with radius and is almost zero in the outermost radial bin (Fig. 10). This is consistent with the BIC values shown for the outer radial bin, which favours the one-component model (Table 4).

8 STELLAR SURFACE MASS DENSITY

Using equation (1) with $f = 1/2\pi$ (isothermal model, see appendix 1 in An18) and measured h_z (Table 2) and σ_z from the hot disc (Table 5, column 2), we calculate the total surface mass density (Σ_{T}) in each radial bin (Table 5, column 3).

The stellar mass surface density of the hot disc (Σ_{D}) is $\Sigma_{\mathrm{D}} = \Sigma_{\mathrm{T}} - (\Sigma_{\mathrm{C},*} + \Sigma_{\mathrm{C,gas}})$, where $\Sigma_{\mathrm{C},*} + \Sigma_{\mathrm{C,gas}}$ is the surface density of a cold thin layer made up of the cold thin disc of stars and the gaseous disc of the galaxy. While we can directly measure $\Sigma_{\mathrm{C,gas}}$ (see Fig. 5 and Table 5, column 4), the cold stellar population contribution $\Sigma_{\mathrm{C},*}$ is not known directly from our data. We can write the equation for

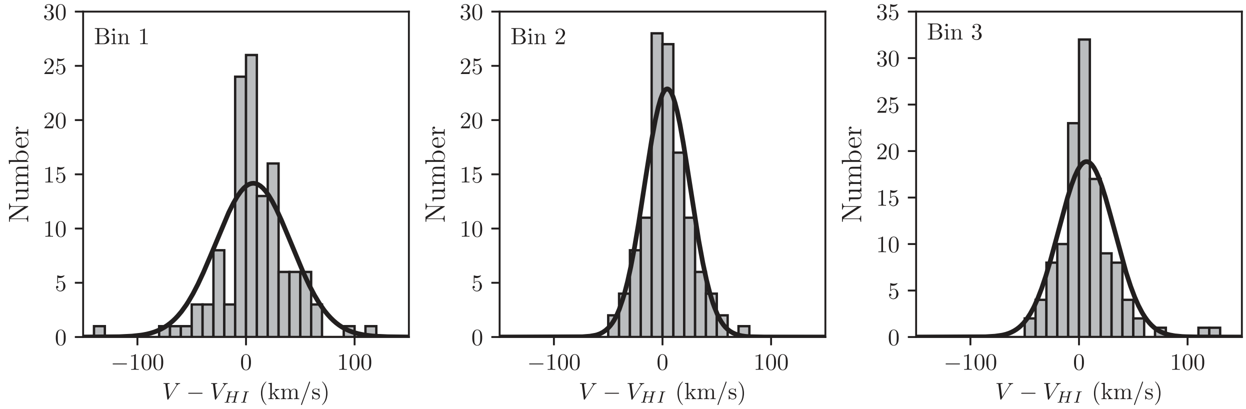

Figure 9. The distribution of the PNe LOS velocities from the bottom panels in Fig. 8 for each radial bin, respectively. The single Gaussian fit to the data is shown with the black curve. The velocity distributions are not well represented by a single Gaussian: the excess of low-velocity PNe is evident.

Table 4. The σ_z values calculated from the PN.S data. We give the 90 per cent confidence upper limit for the cold dispersions. The lower BIC values of the two-component fit suggest it to be the preferred model over the one-component model, except for the outermost radial bin where the one component model is preferred.

Mean radius	Two-component model			One-component model	
(arcsec)	$\sigma_{z,\mathrm{cold}}$ (km s^{-1})	$\sigma_{z,\mathrm{hot}}$ (km s^{-1})	BIC	σ_z (km s^{-1})	BIC
144	$\leq 12.1 \pm 2.3$	32.0 ± 6.4	1236	26.5 ± 1.7	1251
242	$\leq 12.9 \pm 3.3$	20.9 ± 4.1	1076	18.6 ± 1.2	1090
335	$\leq 12.3 \pm 3.5$	14.8 ± 5.9	1062	14.5 ± 1.0	1055

the surface densities of the stellar disc components as

$$\Sigma_{\mathrm{D}} = \frac{\Sigma_{\mathrm{T}} - \Sigma_{\mathrm{C,gas}}}{1 + F_{\mathrm{C}}}, \quad \text{where} \quad F_{\mathrm{C}} = \frac{\Sigma_{\mathrm{C},*}}{\Sigma_{\mathrm{D}}}. \tag{5}$$

We can estimate the ratio of luminosities $L_{\mathrm{C}}/L_{\mathrm{D}}$ of the cold and hot stellar layers from the integrated spectra. These luminosity ratios are given in Table 5 (column 5) for the first two radial positions where the dispersions come from integrated light. From these ratios, we can then estimate the ratios of the surface densities of the cold and hot layers, using stellar population models (Bruzual & Charlot 2003).

We showed in An18 (fig. 12) that the thin disc stars in the solar neighbourhood older than about 3 Gyr have vertical velocity dispersions almost independent of age, at about 20 km s^{-1}. Stars with ages younger than about 3 Gyr show a strong age–velocity dispersion relation, rising from about 10 km s^{-1} for the youngest stars to about 20 km s^{-1} at 3 Gyr. We identify stars with ages >3 Gyr as the old hot population denoted D in Table 5, and stars with ages <3 Gyr as the young cold populations denoted C_* in Table 5.

The age difference of the cold and hot stellar populations is also indicated visually by the spectra of the best-fitting stellar templates used in the spectral fitting analysis (Fig. 7): the colder population looks younger, with its stronger Hβ and (slightly) weaker metallic lines. Fig. 11 shows an extended section of the PPXF spectra including the Hβ region. This region was excluded from the kinematical analysis, thus is not shown in Fig. 7. Three trends are evident in the ratio of the cold/hot spectra: (i) Hβ is stronger in the spectrum for the kinematically colder component, and shows broader wings; (ii) the metallic lines such as the Mgb triplet and the 5270 and 5320 Å Fe-lines are stronger in the kinematically hotter component, and (iii) the continuum for the colder component is somewhat bluer than for the hotter component, as seen by reference to the horizontal dashed line. These three trends are consistent with the colder population being younger, and follow naturally if the mean temperatures of the stars which dominate the spectrum are lower in the hotter component. We note that only the region of spectrum from 5040 to 5310 Å was used in the PPXF fit.

In An18, we then showed that, if the star formation rate in the disc has decayed with time like $\exp(-t/\tau)$, and if $\tau > 3$ Gyr, then the ratio of (*M*/*L* for the cold component) to (*M*/*L* for the hot component) is about 0.167, almost independent of τ. Assuming NGC 6946 has a similar age–velocity relation as in the solar neighbourhood, i.e. the old thin disc is composed of stars with ages between 3 and 10 Gyr and assuming a star formation rate that decays with time like $\exp(-t/\tau)$, then we can derive the ratio of surface densities of young and old populations given as F_{C} in Table 5 (column 6) for the first two radial positions. For the three radial positions using PNe as tracers (R = 4.3–9.9 kpc), we cannot use these arguments, because of possible contamination of the sample by H II regions, and because the lifetimes of PNe vary strongly with progenitor mass (Miller Bertolami 2016). For columns 5 and 6 of Table 5, we therefore adopt the means of the values found from our integrated light spectra in the first two radial positions. The values of Σ_{D} and $\Sigma_{\mathrm{C},*}$ in columns 7 and 8 follow from equation (5). The errors for Σ_{T}, shown in Table 5 are relatively large (30–40 per cent for most radial bins) – these errors include errors in all spectroscopic and photometric parameters (scale length and scale height) used to evaluate Σ_{T}, and therefore following simple error propagation overestimates the relative errors between radial bins.

Table 5 (columns 9–12), gives the total stellar *M*/*L* ratios for ($\Sigma_{\mathrm{D}} + \Sigma_{\mathrm{C},*}$) at each radius in *BVI* and 3.6 μm photometric bands (Fig. 4). Prior to derivation of the *M*/*L* ratio, all photometric magnitudes were corrected for the Galactic extinction and inclination effects. From Table 5, it is visible that values of the mass-to-light ratio (*M*/*L*, $\Upsilon_\star$) vary with radius in every band differently from some previous studies (Martinsson et al. 2013; Swaters et al. 2014). In our approach, even if the light declines in the same way as mass ($h_{\mathrm{phot}} = h_{\mathrm{dyn}}$), the ratio of the cold-to-hot component and the contribution from gas mass also changes with radius, contributing to radial variation of the *M*/*L* values. However, we also do not exclude the contribution of the observational errors to this radial change in *M*/*L*. Interestingly, the mean value of the $\Upsilon_\star[3.6]$ is equal to 0.4, which is lower in comparison with the current stellar population models that assume constant $\Upsilon_\star[3.6] = 0.6$ (Meidt et al. 2012; Röck et al. 2015). This lower value of $\Upsilon_\star[3.6]$ can be explained with the very high star

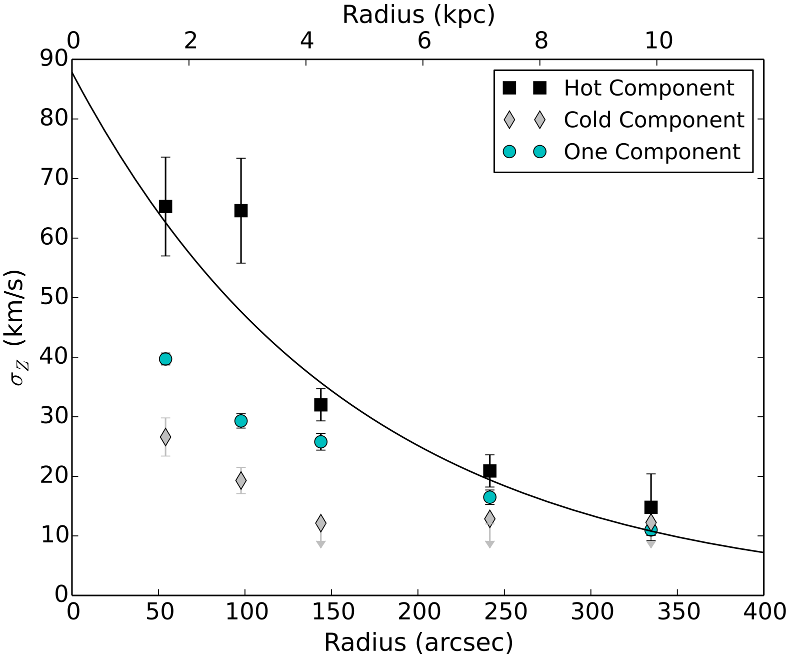

Figure 10. The vertical velocity dispersion as a function of radius in NGC 6946. The black and grey markers indicate the hot and cold velocity dispersions, respectively, from our two-component fits, the cyan markers are our single-component values. The two inner data points at $R = 54$ and 98 arcsec were obtained for integrated light spectra from VIRUS-W and the outer data points are for PNe from PN.S. The solid line denotes an exponential with twice the galaxy's dynamical scale length ($h_{\rm dyn} = 92$ arcsec = 2.72 kpc) fit to the hot component. Our data have been corrected for the H I velocity dispersion and PNe measuring errors. The cold component from the PN.S data was dominated by our errors, and we show the 90 per cent upper limits for these values. The errors bars are the 1σ errors obtained from Monte Carlo simulations.

Table 5. Parameters for NGC 6946 at the five radii where the velocity dispersion of the hot disc was measured (inner two radii from integrated light, outer three from PNe). All surface densities are in units of $M_\odot$ pc^{-2}. The columns are (1) radius (kpc); (2) vertical velocity dispersion σ_z of the hot disc; (3) total surface density Σ_T from equation (2); (4) observed surface density $\Sigma_{C,\rm gas}$ of the gas layer; (5) ratio of luminosities of cold and hot layers from the integrated spectra in rows 1 and 2, and adopted mean of rows 1 and 2 in rows 3–5; (6) the ratio F_C of the stellar surface densities of the cold and hot layers from Bruzual & Charlot (2003); (7) the surface density Σ_D of the hot layer from equation (5); (8) the stellar surface density $\Sigma_{C,*}$ of the cold layer; (9)–(12) total ($\Sigma_D + \Sigma_{C,*}$) stellar *M*/*L* ratio in *BVI* and 3.6 μm bands. We note the absence of the last measured point of the $\Upsilon_\star$ in optical bands as our data do not extend far enough.

R (kpc) (1)	σ_z (km s^{-1}) (2)	Σ_T ($M_\odot$ pc^{-2}) (3)	$\Sigma_{C,\rm gas}$ ($M_\odot$ pc^{-2}) (4)	L_C/L_D (5)	F_C (6)	Σ_D ($M_\odot$ pc^{-2}) (7)	$\Sigma_{C,*}$ ($M_\odot$ pc^{-2}) (8)	$\Upsilon_\star$ [*B*] (9)	$\Upsilon_\star$ [*V*] (10)	$\Upsilon_\star$ [*I*] (11)	$\Upsilon_\star$ [3.6] (12)
1.6	65.3	420 ± 152	25.5 ± 4	52/48	0.18	334.32	60.17	2.48 ± 0.9	2.36 ± 0.85	1.31 ± 0.47	0.48 ± 0.17
2.9	64.6	411 ± 157	17.7 ± 4	46/54	0.14	345.0	48.3	3.61 ± 1.2	3.61 ± 1.2	2.07 ± 0.69	0.72 ± 0.24
4.3	32.0	101 ± 31	14.3 ± 5	49/51	0.16	74.74	11.95	1.1 ± 0.34	1.1 ± 0.34	0.73 ± 0.23	0.26 ± 0.12
7.2	20.9	43 ± 16	8.3 ± 4	49/51	0.16	29.91	4.78	0.91 ± 0.34	1.12 ± 0.41	0.74 ± 0.28	0.29 ± 0.12
9.9	14.8	21.5 ± 19	5.2 ± 5	49/51	0.16	14.05	2.24	–	–	–	0.47 ± 0.4

formation rate for this galaxy (4.76 $M_\odot$ yr^{-1}; Walter et al. 2008). As was shown by Querejeta et al. (2015), the flux of the Spitzer 3.6 μm band represents not only the light from the old stellar population, but also that emitted by the warm dust heated by young stars and re-emitted at longer wavelengths, and its contribution can be as high as 30 per cent at the regions of high star formation activity. Moreover, AGB stars also peak at 3.6 μm, significantly contributing into the total flux, but not into the stellar mass of a galaxy. Ponomareva et al. (2017) also shown that the use of the 3.6 μm luminosities corrected for the non-stellar contamination can even decrease the scatter in the Tully–Fisher relation. Thus, if we assume the non-stellar contamination of ~30 per cent for NGC 6946, the values of the $\Upsilon_\star$[3.6] will increase towards the mean value of ~0.7. Moreover, the mean value of $\Upsilon_\star$[3.6] = 0.4 is in agreement with the $\Upsilon_\star$[3.6] derived as a function of the [3.6]–[4.5] colour for a sample of spiral galaxies (Ponomareva et al. 2018, see equation 13). In comparison with NGC 628 (An18), we find the mean $\Upsilon_\star$ to be lower for the NGC 6946 independently of a photometrical band. This is consistent with the difference in total star formation rate between the two galaxies: Walter et al. (2008) give the SFR for NGC 628 as 1.21 $M_\odot$ yr^{-1} and for NGC 6946 as 4.76 $M_\odot$ yr^{-1}, indicating that the stellar population in NGC 628 is likely to be older in the mean. This is also consistent with the above-mentioned non-stellar contamination in the 3.6 μm band.

9 ROTATION CURVE DECOMPOSITION

9.1 Observed H I rotation curve

We derive the observed rotation curve of NGC 6946 using THINGS data (Walter et al. 2008). As the galaxy is large and well-resolved, we use the 2D tilted-ring modelling approach (Begeman 1989) to

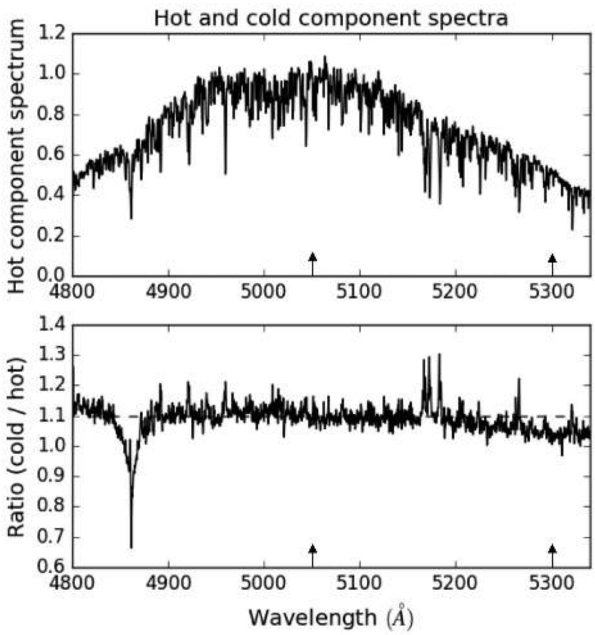

Figure 11. The upper panel shows the spectrum for the hot component for the inner radial zone in NGC 6946. The lower panel shows the ratio of the cold to the hot spectra, pixel by pixel. The spectral region between 5050 and 5300 Å used for the fit is indicated with vertical arrows. The [N I] emission lines at ∼5200 Å have been omitted from the fit.

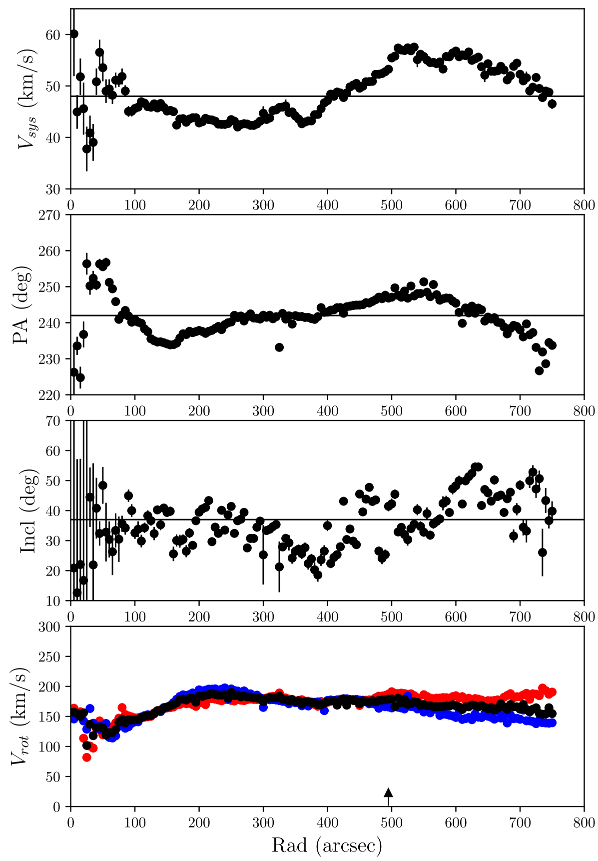

Figure 12. Kinematic fits to the H I THINGS data for NGC 6946. The top three panels show the systemic velocity, position angle, and inclination as a function of radius. The black solid lines indicate the average values that were used in the fit for the rotational velocity. The bottom panel shows the H I rotation curve of the galaxy. The blue and red data points are for the approaching and receding side of the galaxy, respectively. The black curve is the average rotation curve for both sides. The optical radius ($R_{\rm opt} \sim 3.2\, h_{\rm R}$) of the galaxy is indicated with the black arrow.

derive the rotation curve from the observed velocity field. First, the velocity field was constructed using the Gauss–Hermit polynomial fitting function and then corrected for the skewed velocity profiles that reflect random motions (Ponomareva et al. 2016). The results of the tilted-ring modelling are shown in Fig. 12. We find the position and inclination angles to be 242 and 37 degrees, respectively. We fix these values to derive the final rotation curve for the receding and approaching sides of the galaxy, shown in the bottom panel of Fig. 12. It is clear that the rotation curve of NGC 6946 is well-behaved, reaching the flat part at ∼170 arcsec. The difference between the approaching and receding sides of the rotation curve was adopted as the error on the rotational velocity.

9.2 Stellar distribution

The rotation curve and the 3.6 μm surface brightness profile of NGC 6946 indicate the presence of the small bulge component. As our spectral observations do not cover the central region of the galaxy, the bulge does not contribute to the derived total surface mass density. Therefore, to include the contribution from the bulge to the total observed rotation curve, we fit the bulge component to the 3.6 μm profile (Fig. 4) and then convert its luminosity into mass using $\Upsilon_\star[3.6] = 0.6$ (Meidt et al. 2012; Querejeta et al. 2015; Röck et al. 2015).

Thus, we have all of the baryonic components contributions and we model their rotation curves using a spherical potential for the bulge and the exponential total disc component, using the derived central surface mass density ($\Sigma_0 = 758.84 \pm 162$ M$_\odot$ pc^{-2}), dynamical scale length ($h_{\rm dyn} = 2.72$ kpc) and *I*-band scale height ($h_z = 376$ pc), inferred from the measured *I*-band scale length (Section 4). We model the rotation curves of all the baryonic components with the same radial sampling as was used for the derivation of the observed rotation curve.

9.3 Mass modelling

The total rotational velocity of a spiral galaxy can be presented as the quadratic sum of the rotational velocity for its baryonic components and a dark halo:

$$V^2_{\rm tot} = V^2_{\rm bar} + V^2_{\rm halo}, \quad (6)$$

where $V_{\rm bar}$ is the rotational velocity of the baryonic components of a galaxy (stars and gas) and $V_{\rm halo}$ is the velocity of a DM halo. From our analysis, we have direct measurements on all baryonic components of the disc, using dynamically obtained surface mass density, and of the bulge from the 3.6 μm profile. Thus, we can model the total baryonic rotational velocity curve and then fit the rotation curve of the DM halo so that $V_{\rm tot}$ matches $V_{\rm obs}$ as closely as possible. Since we have directly measured total surface mass density of the disc, we do not have the usual uncertainties related to the disc *M*/*L* that are a major concern in decomposing rotation curves.

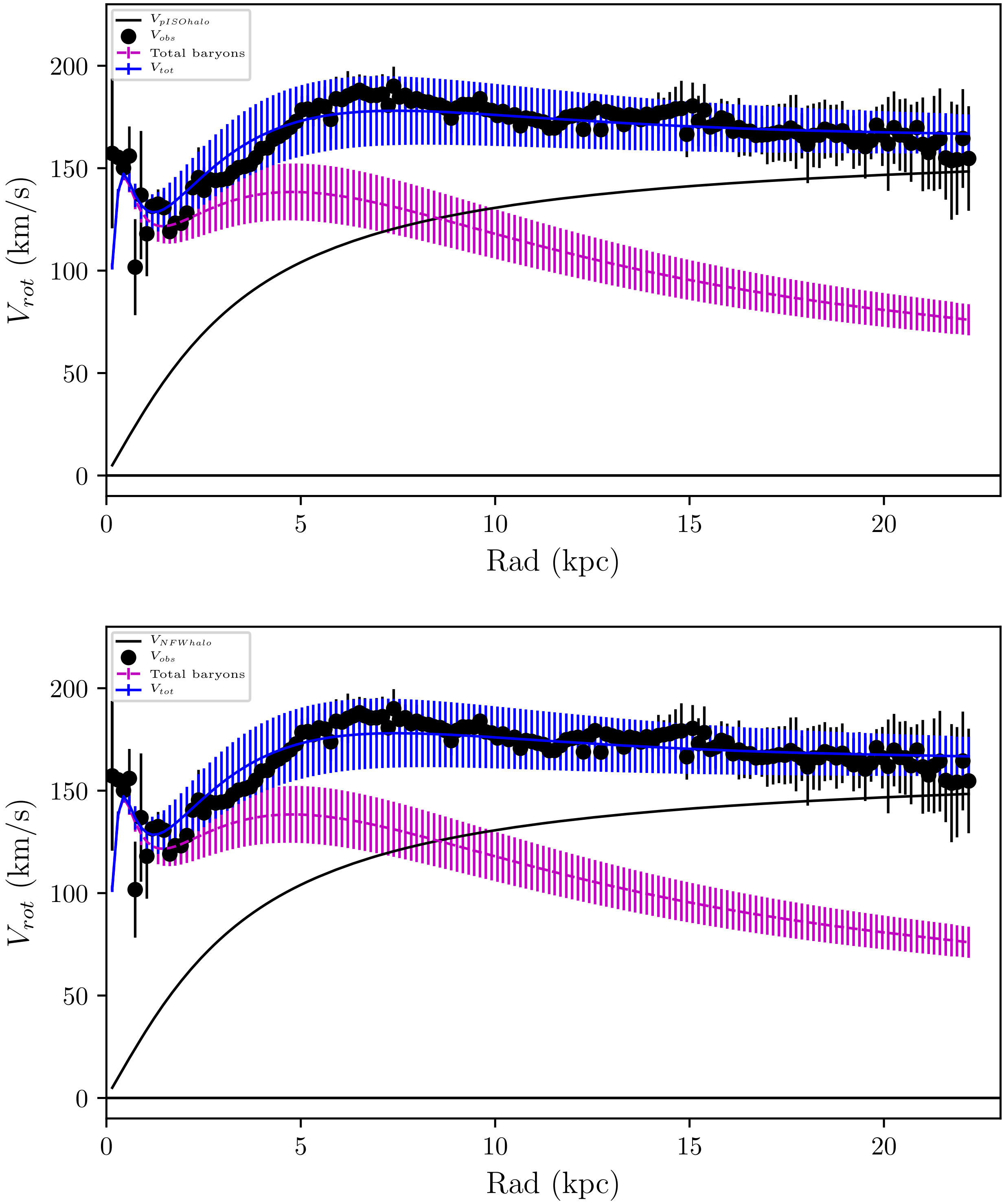

Figure 13. The rotation curve decomposition for NGC 6946 by fitting a pISO halo (top panel) and an NFW halo (bottom panel). The observed H I rotation curve is shown as black dots. The magenta dashed line is the rotation curve from the total baryonic component: bulge + gas + disc with the 1σ errors. The blue line represents the total rotational velocity: $V_{\rm tot}^2 = V_{\rm bar}^2 + V_{\rm halo}^2$. The short blue vertical lines show the 1σ errors of the modelled total rotational velocity. 1kpc = 33.8 arcsec.

We estimate the maximum rotational velocity of the baryonic rotation curve (blue line in Fig. 13) at $2.2\,h_{\rm dyn}$ to be equal to $V_{\rm max}({\rm bar}) = 130\,{\rm km\,s^{-1}}$ with the typical error of 13 per cent due to the error on the central surface brightness and the negative covariance between the $h_{\rm R,dyn}$ and the $\sigma_z(0)$ (see An18 for more details). In comparison with the maximum velocity of the total rotation curve at $2.2\,h_{\rm dyn}$ ($V_{\rm max} = 170 \pm 10\,{\rm km\,s^{-1}}$), we find our disc to be closer to maximal with $V_{\rm max}({\rm bar}) = 0.76(\pm 0.14)V_{\rm max}$.

Table 6. The derived parameters of the fitted DM haloes from the mass modelling. Solely based on the value of the χ^2_{red}, the pISO model may be a better fit to the data.

pISO			NFW		
R_C (kpc)	ρ (10^{-3} M$_\odot$ pc^{-3})	χ^2_{red}	C	R_{200} (kpc)	χ^2_{red}
2.8 ± 0.2	57.6 ± 8	0.93	10.8 ± 1	169.3 ± 7	1.1

For our further analysis, we use two different DM halo models: the pseudo-isothermal (pISO) and the NFW halo. The pISO halo rotation curve is parametrized by its central core density ρ_0 and its core radius R_c:

$$V_{DM}^{pISO}(R) = \sqrt{4\pi G \rho_0 R_c^2 \left[1 - \frac{R_c}{R}\tan^{-1}\left(\frac{R}{R_c}\right)\right]}, \quad (7)$$

while the NFW halo (Navarro, Frenk & White 1997) is parametrized by its circular velocity V_{200} at the virial radius R_{200} and its central concentration c:

$$V_{DM}^{NFW}(R) = V_{200}\left[\frac{\ln(1+cx) - cx/(1+cx)}{x[\ln(1+c) - c/(1+c)]}\right]^{1/2}, \quad (8)$$

where $x = R/R_{200}$.

Thus, we keep the rotation curve of the baryons fixed, and use the GIPSY (van der Hulst et al. 1992) task ROTMAS to fit the rotation curves for the dark haloes. The results from this modelling is presented in Fig. 13 (the top panel is for the pISO halo and the bottom panel for the NFW halo). The derived parameters of the fitted DM rotation curves are presented in Table 6. The error on the total rotational velocity (blue line in Fig. 13) follows from the error on the central surface density. Although the rotation curve shapes for the pISO and NFW haloes are similar, the pISO rotation curve is a slightly better fit, with $\chi^2_{red} = 0.93$ versus $\chi^2_{red} = 1.1$ for the NFW halo.

Fig. 14 shows the χ^2 maps of the 2D parameter space between the main parameters of the DM haloes. It is clear that derived dark halo parameters for the pseudo-isothermal and NFW models have significant covariance: the coloured ellipses in each panel represent the 1σ–5σ values from inside to outside. The errors quoted in Table 6 are the 1σ uncertainties.

10 CONCLUSIONS

We use absorption line spectra in the inner regions and PNe in the outer regions of the galaxy NGC 6946 to trace the kinematics of the disc. We show that there exists a younger, kinematically colder population of tracers within an older and hotter component.

When attempting to break the disc–halo degeneracy by measuring the surface mass density of the disc, using the velocity dispersion and the estimated scale height of the disc, it is crucial that the dispersion and the scale height pertain to the same population of stars. The scale height, obtained from near-IR studies of edge-on galaxies is for the older population of thin disc stars. We use this scale height with the dispersion of the hotter component to calculate the surface mass density. This density is a factor of 2.3 times greater than the surface density we would get if we assume a single homogeneous population of tracers. This factor is large enough to make the difference between concluding that a disc is maximal or submaximal.

We find that the observed vertical velocity dispersion of the hotter component follows an exponential radial decrease. In comparison, the central velocity dispersions for the hot components in NGC 628

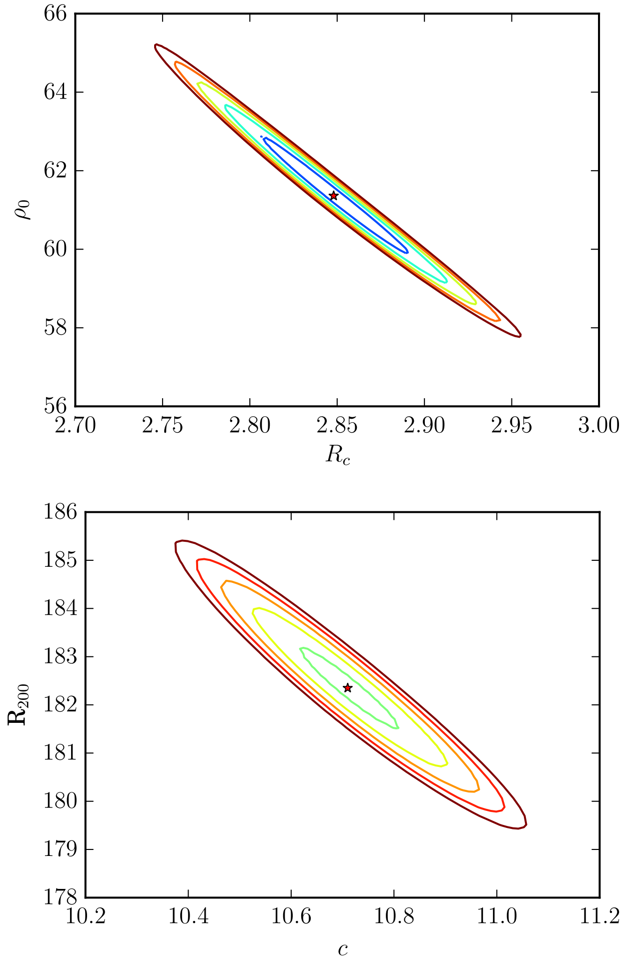

Figure 14. χ^2 map in the 2D parameter space of the dark halo parameters. The upper panel shows the covariance between the density and radius of the core of the pISO model of the dark halo. The lower panel shows the covariance between the virial radius and concentration of the NFW dark halo model. The ellipses represent the 1σ–5σ values from inside out.

and NGC 6946 do not differ by much: 73.6 ± 9.8 km s^{-1} for NGC 628 and 87.8 ± 4.9 km s^{-1} for NGC 6946. The *B*-band magnitudes from Walter et al. (2008), −19.97 and −20.61, respectively, suggest that the brighter galaxy has a higher central σ_z.

The dynamical scale length of the galaxy (derived by fitting $\sigma_z(R) = \sigma_z(0)\exp(-R/2h_{dyn})$ to the hot component velocity dispersions in Fig. 10) agrees well with the photometric scale length of the galaxy (derived by fitting $I(R) = I(0)\exp(-R/h_{r,[3.6]})$ to the 3.6 μm surface brightness distribution in Fig. 4). In this case, the expected *M*/*L* in this galaxy should be close to constant over the radial region probed by our study (see Section 8). We find that in all four photometric bands (*BVI* and 3.6 μm), the *M*/*L* varies with radius, but within the errors being consistent with a radially constant value. Moreover, we find that *M*/*L* in the 3.6 μm band has a lower value than assumed by single stellar population models (Meidt et al. 2012; Querejeta et al. 2015; Röck et al. 2015). Interestingly, its mean value over all radii agrees well with the $\Upsilon_\star$[3.6] derived as a function of the [3.6]–[4.5] colour for a sample of spiral galaxies (Ponomareva et al. 2018). We suggest that lower values of the $\Upsilon_\star$[3.6] are due to the contamination from dust and AGB stars of the 3.6 μm flux. The maximum correction of 30 per cent (Querejeta et al. 2015) would increase the mean $\Upsilon_\star$[3.6] by a factor of two.

Decomposing the rotation curve of this galaxy, after taking into account the hot and cold stellar components, leads to a maximal disc ($V_{\max}(\mathrm{bar}) = 0.76(\pm 0.14)V_{\max}$). The disc contributes about 76 per cent of the rotation curve at its peak, which is consistent with our previous study of NGC 628 (78 per cent). The molecular gas makes an unusually large contribution in the inner parts of this galaxy, and the baryons together dominate the radial component of the gravitational field out to a radius of about 8 kpc.

ACKNOWLEDGEMENTS

We thank Maximilian Fabricius for his help with the VIRUS-W data reduction and analysis. We thank the anonymous referee for comments and suggestions that significantly improved this paper. We acknowledge comments and suggestions from Matthew Bershady. SA would like to thank ESO for the ESO studentship that helped support part of this work. AAP, KCF, MA, and OEG acknowledge the support of the Australian Research Council Discovery Project grant DP150104129. AAP acknowledges the support of the **Science and Technology Facilities Council** (STFC) consolidated grant ST/S000488/1, the VICI grant 016.130.338 of the Netherlands Foundation for Scientific Research (NWO), and the Leids KerkhovenBosscha Fonds (LKBF) for travel support. The authors are very grateful to the staff at McDonald Observatory for granting the observing time and support on the 107 inch telescope. The authors would also like to thank the Isaac Newton Group staff on La Palma for supporting the PN.S over the years, and the Swiss National Science Foundation, the Kapteyn Institute, the University of Nottingham, and INAF for the construction and deployment of the H α arm.

DATA AVAILABILITY

All data used in this paper are available on request to the corresponding authors.

REFERENCES

Anand G. S., Rizzi L., Tully R. B., 2018, AJ, 156, 105
Aniyan S., Freeman K. C., Gerhard O. E., Arnaboldi M., Flynn C., 2016, MNRAS, 456, 1484
Aniyan S. et al., 2018, MNRAS, 476, 1909 (An18)
Begeman K. G., 1989, A&A, 223, 47
Bershady M. A., Verheijen M. A. W., Swaters R. A., Andersen D. R., Westfall K. B., Martinsson T., 2010a, ApJ, 716, 198
Bershady M. A., Verheijen M. A. W., Westfall K. B., Andersen D. R., Swaters R. A., Martinsson T., 2010b, ApJ, 716, 234
Bershady M. A., Martinsson T. P. K., Verheijen M. A. W., Westfall K. B., Andersen D. R., Swaters R. A., 2011, ApJ, 739, L47
Bhattacharya S. et al., 2019, A&A, 631, A56
Boomsma R., Oosterloo T. A., Fraternali F., van der Hulst J. M., Sancisi R., 2008, A&A, 490, 555
Bottema R., van der Kruit P. C., Freeman K. C., 1987, A&A, 178, 77
Bruzual G., Charlot S., 2003, MNRAS, 344, 1000
Cappellari M., 2017, MNRAS, 466, 798
Conroy C., Gunn J. E., White M., 2009, ApJ, 699, 486
Cortesi A. et al., 2013, MNRAS, 432, 1010
Crosthwaite L. P., Turner J. L., 2007, AJ, 134, 1827
de Grijs R., Peletier R. F., van der Kruit P. C., 1997, A&A, 327, 966
Douglas N. G. et al., 2002, PASP, 114, 1234
Douglas N. G. et al., 2007, ApJ, 664, 257
Fabricius M. et al., 2012, in McLean I. S., Ramsay S. K., Takami H., eds, Proc. SPIE Conf. Ser. Vol. 8446, Ground-based and Airborne Instrumentation for Astronomy IV. SPIE, Bellingham, p. 84461O
Goessl C. A. et al., 2006, in Silva D. R., Doxsey R. E., eds, Proc. SPIE Conf. Ser. Vol. 6270, Observatory Operations: Strategies, Processes, and Systems. SPIE, Bellingham, p. 627021
Herrmann K. A., Ciardullo R., 2009a, ApJ, 703, 894
Herrmann K. A., Ciardullo R., 2009b, ApJ, 705, 1686
Herrmann K. A., Ciardullo R., Feldmeier J. J., Vinciguerra M., 2008, ApJ, 683, 630
Kormendy J., Freeman K. C., 2016, ApJ, 817, 84
Kreckel K., Groves B., Bigiel F., Blanc G. A., Kruijssen J. M. D., Hughes A., Schruba A., Schinnerer E., 2017, ApJ, 834, 174
Kregel M., van der Kruit P. C., de Grijs R., 2002, MNRAS, 334, 646
Kregel M., van der Kruit P. C., Freeman K. C., 2005, MNRAS, 358, 503
Lee J. C., 2006, PhD thesis, Univ. Arizona
Leroy A. K. et al., 2009, AJ, 137, 4670
Macciò A. V., Ruchayskiy O., Boyarsky A., Muñoz-Cuartas J. C., 2013, MNRAS, 428, 882
Makarova L., 1999, A&AS, 139, 491
Maraston C., 2005, MNRAS, 362, 799
Martinsson T. P. K., Verheijen M. A. W., Westfall K. B., Bershady M. A., Andersen D. R., Swaters R. A., 2013, A&A, 557, A131
Meidt S. E. et al., 2012, ApJ, 744, 17
Miller Bertolami M. M., 2016, A&A, 588, A25
Muñoz-Mateos J. C. et al., 2009, ApJ, 703, 1569
Navarro J. F., Frenk C. S., White S. D. M., 1997, ApJ, 490, 493
Ponomareva A. A., Verheijen M. A. W., Bosma A., 2016, MNRAS, 463, 4052
Ponomareva A. A., Verheijen M. A. W., Peletier R. F., Bosma A., 2017, MNRAS, 469, 2387
Ponomareva A. A., Verheijen M. A. W., Papastergis E., Bosma A., Peletier R. F., 2018, MNRAS, 474, 4366
Pulsoni C. et al., 2018, A&A, 618, A94
Querejeta M. et al., 2015, ApJS, 219, 5
Röck B., Vazdekis A., Peletier R. F., Knapen J. H., Falcón-Barroso J., 2015, MNRAS, 449, 2853
Schlafly E. F., Finkbeiner D. P., 2011, ApJ, 737, 103
Schwarz G., 1978, Ann. Stat., 6, 461
Shapiro K. L., Gerssen J., van der Marel R. P., 2003, AJ, 126, 2707
Somerville R. S. et al., 2018, MNRAS, 473, 2714
Swaters R. A., Bershady M. A., Martinsson T. P. K., Westfall K. B., Andersen D. R., Verheijen M. A. W., 2014, ApJ, 797, L28
van Albada T. S., Bahcall J. N., Begeman K., Sancisi R., 1985, ApJ, 295, 305
van der Hulst J. M., Terlouw J. P., Begeman K. G., Zwitser W., Roelfsema P. R., 1992, in Worrall D. M., Biemesderfer C., Barnes J., eds, ASP Conf. Ser. Vol. 25, Astronomical Data Analysis Software and Systems I. Astron. Soc. Pac., San Francisco, p. 131
van der Kruit P. C., Freeman K. C., 1984, ApJ, 278, 81
Walter F., Brinks E., de Blok W. J. G., Bigiel F., Kennicutt R. C., Jr., Thornley M. D., Leroy A., 2008, AJ, 136, 2563

This paper has been typeset from a TEX/LATEX file prepared by the author.